Lasers in Medical Science (2019) 34:561–569
https://doi.org/10.1007/s10103-018-2630-6

ORIGINAL ARTICLE

Visualize and quantify the structural alteration of the rat spinal cord injury based on multiphoton microscopy

Chenxi Liao[1] · Xiaoqin Zhu[1] · Linquan Zhou[2] · Zhenyu Wang[2] · Wenge Liu[2] · Jianxin Chen[1]

Received: 31 May 2018 / Accepted: 28 August 2018 / Published online: 9 September 2018

Abstract

The development of imaging technique to visualize and quantify the structural alteration of the spinal cord injury (SCI) may lead to better understanding and treatments of the injuries. In this work, multiphoton microscopy (MPM) based on two-photon excited fluorescence (TPEF) and second-harmonic generation (SHG) was tentatively applied to quantitatively visualize the cellular microstructures of SCI to demonstrate the feasibility and superiority of MPM in SCI imaging. High-contrast MPM images of normal and injured spinal cord tissue were obtained for comparison. Moreover, the changes of injured spinal cord were characterized by the quantitative analysis of the MPM images. These results showed that MPM combined with quantitative method has the ability to identify the characteristics of spinal cord injury including the changes in the contents of nerve fibers and extracellular matrix. With the advancement of MPM, we believe that this technique has great potential to provide the histological diagnosis for the monitoring and evaluation of SCI.

Keywords Multiphoton microscopy (MPM) · Two-photon excited fluorescence (TPEF) · Second-harmonic generation (SHG) · Spinal cord injury (SCI)

Introduction

The spinal cord is an integral part of the central nervous system (CNS). It is a complex organ containing various cellular structures, including various types of nerves and glial cells, strictly aligned long nerve fibers and fiber tracts, endothelial cells, and vessels. The region in which nerve fibers lie is called "white matter," and it is very rich in phospholipids and cholesterol. The neuronal cell bodies make up the "gray matter," which lies in a butterfly-shaped region in the center of the spinal cord [1]. In addition, the extracellular matrix (ECM) is highly organized that mainly includes chondroitin sulfate proteoglycans, hyaluronan link proteins, and tenascin-R. ECM provides structure and organization to tissues and helps to regulate cell migration and intercellular communication [2, 3]. The injury to the spinal cord involves a number of processes and leads to progressive damage of nervous tissue. It causes massive neuronal death and reactive astrogliosis, accompanied by a temporally and spatially orchestrated inflammatory response. The ECM compositions are also changing and the primarily loose meshwork structure is broken down and fragmented [4].

Many efforts to understand and treat the spinal cord injury (SCI) have been undertaken in recent years, including the development of better imaging techniques to provide pertinent microstructural information of SCI and to direct the use of pharmacological regenerative therapies for reducing damage [5, 6]. Traditional modalities such as plain radiography, computed tomography (CT), and magnetic resonance imaging (MRI), provide excellent macrostructural information to guide the patient management. A variety of novel advanced imaging techniques are developed to principally present the microstructural function of the spinal cord, including diffusion tensor imaging (DTI), magnetic resonance spectroscopy (MRS), positron emission tomography (PET), single-photon emission computed tomography (SPECT), and functional MRI (fMRI) [7–9]. However, there are some disadvantages and limitations

✉ Xiaoqin Zhu
zhuxq@fjnu.edu.cn

✉ Zhenyu Wang
876744032@qq.com

[1] Key Laboratory of OptoElectronic Science and Technology for Medicine of Ministry of Education, Fujian Provincial Key Laboratory of Photonics Technology, Fujian Normal University, Fuzhou 350007, China

[2] Department of Orthopedics, Affiliated Union Hospital of Fujian Medical University, Fuzhou 350001, People's Republic of China

of these imaging modalities, including low resolution, poor contrast sensitivity, and necessity for contrast medium.

Recently, multiphoton microscopy (MPM) has exhibited the ability to detect biological tissue architecture and changes in these tissues at the cellular and subcellular levels with high resolution and high sensitivity. Based on two-photon excited fluorescence (TPEF) and second-harmonic generation (SHG), MPM allows visualizing the cells and ECM by excitation of intrinsic fluorescent molecules [10]. TPEF is a nonlinear process well-suited for high-resolution imaging of intrinsic molecular signals from elastin and cells [11]. SHG enables direct imaging of anisotropic biological structures of collagen by interacting with highly non-centrosymmetric molecular assemblies and it has been demonstrated to quantitate collagen after nerve repair via fiber alignment [12]. Compared to other microscopy techniques, MPM has several unique advantages such as the enhancement of imaging depths and reduction of photodamage. In our study, we attempt to identify the microstructure of injured spinal cord by using MPM. And the morphological features were quantitatively analyzed based on the MPM images to characterize the alterations following SCI.

Materials and methods

Spinal cord injury

All animal experiments were approved by the Animal Care and Use Committee in Fujian Medical University. Six eight-week-old Sprague-Dawley rats (250–280 g) were purchased from Fujian Medical University Laboratory Animal Center. Rats were housed in a clean-room facility with 12-h light/dark cycles and free access to chow and water. They were allocated into two groups: SCI ($n = 3$) and control ($n = 3$) groups. A standardized contusion injury was produced with a weight-drop technique [13]. The rats of SCI group were anesthetized with an intraperitoneal injection of 10% chloral hydrate (3.3 ml/kg). A laminectomy was performed at the T10 level of the vertebral column providing a circular opening of about 3-mm diameter. Angled Allis clamps were attached at the spinous processes of T9 and T11 to stabilize the animal. The impounder of the weight-drop device was lowered onto the exposed dura and a 20-g weight was dropped onto the dura from a height of 1 cm. The transverse diameter of the injured area is 2 mm.

Sample preparations

At 24 h after SCI, the injured rats were perfused with saline (300 ml over 3–4 min) followed by fixative (300 ml 4% paraformaldehyde buffer over 3–4 min). A 1-cm segment of spinal cord centered on the injury site was removed and then processed using 10% buffered formalin fixation, alcohol dehydration, and paraffin embedding. Control tissues were from the T10 level of normal, uninjured sex, and age-matched rats that were similarly processed.

The spinal cord tissues were divided into two parts: one part was sectioned perpendicular to the axial direction and the other part was sectioned in parallel to the axial direction of the vertebral column. Each part was cut into five consecutive sections of 10-μm thickness using a microtome. Four of five consecutive sections were used for MPM imaging. MPM-imaged sections were deparaffinized with xylene and alcohol and sandwiched between a glass slide and cover slip prior to imaging.

The middle sections were stained with H&E according to standard procedures for histological examination and reviewed by a certified pathologist. They were imaged using a standard bright field light microscope (Eclipse Ci-L, Nikon Instruments Inc., Japan) with a CCD camera (Nikon, DS-Fi2, Japan). The obtained histological images were compared to MPM results for confirmation of the structures and cells.

Imaging system

The multiphoton microscopic imaging system used in this study contained a high-throughput scanning inverted Axiovert 200 microscope (LSM 510 META; Zeiss, Jena, Thuringia, Germany) [14]. In addition, it contained a mode-locked femtosecond Ti: sapphire laser (110 fs, 76 MHz), tunable from 700 to 980 nm (Mira 900-F; Santa Clara, Coherent, America). The polarization of laser light is linear. A Plan-Apochromat oil immersion objective (×63, NA = 1.4, Zeiss) was employed for high-resolution imaging of spinal cord samples. The META detector was used to detect all signals in backscattered geometry and consisted of a high-quality, reflective grating and an optimized 32-channel photomultiplier tube (PMT) array detector. All 32 PMT of the detector covered a spectral width ranging from 377 to 719 nm, and a single PMT covered a spectral range of 10.7 nm. The morphology of spinal cord was imaged via two different channels: SHG images of collagen or nerve fibers were extracted from 389 to 419 nm using one of the channels, while TPEF images of cells were isolated from 430 to 716 nm using another channel. Pseudo-colors of green (for SHG images) and red (for TPEF images) were applied using the software. The images (512 × 512 pixels) were obtained at a rate of 2.56 μs per pixel. An optional HRZ 200 fine focusing stage (Carl Zeiss) was used to move the motorized x–y scanning stage for obtaining a large-scaled image. All images were obtained from an accumulation of 16 scans and had an 8-bit pixel depth.

Quantitative analysis

In order to quantitatively assess the alteration of white matter in normal and injury spinal cord in the transverse sections, the cavity density and ECM content were analyzed. The cavity density was measured by the ImageJ software (version

1.43 m). And the ECM content was defined as the ratio of the TPEF pixels over the whole pixels in each image to show the variation of ECM. In detail, for each TPEF image, the number of TPEF pixels were defined as *A* which can be measured by setting the appropriate threshold of the intensity values, and the total number of pixels in the image were defined as *B*. Then, the ECM content was calculated according to the following formula: *A*/*B*. Furthermore, in the longitudinal spinal cord sections, the injury in white matter was evaluated by ECM orientation and ECM content. ECM orientation was quantified by a weighted orientation vector summation algorithm performed by Matlab software (version R2012b). This automated image analysis approach is recently developed for the rapid quantification of fiber alignment at each pixel within images [15].

Quantitative data were summarized as the mean and standard deviation (SD), shown as "mean ± SD". Each of the data groups was tested using the Shapiro-Wilk test, and data followed a Gaussian distribution when the *p* value was greater than 0.05 [16]. The two-tailed Student's *t* test was used to determine whether there were significant differences between groups. Differences were considered to be statistically significant when the *p* values were less than 0.05. All statistical analyses were performed using SPSS software (version 16.0).

Results and discussion

Multiphoton imaging and quantifying the transversal spinal cord sections

To demonstrate the microstructural alteration of the injured spinal cord, the representative MPM images and the corresponding H&E-stained images from the transverse sections of normal and injured spinal cords are shown in Fig. 1. In the MPM images, cells and ECM produce TPEF signals (red color-coded), whereas the collagen generates strong SHG signals (green color-coded). In Fig. 1a, the large-scaled MPM image from the transverse section of normal spinal cord shows an obvious H-shaped gray matter completely enveloped by the white matter due to their different components. And the spinal pia mater (Fig. 1, arrowhead), mainly composed of types I and III collagen [17], closely follows and encloses the curves of the spinal white matter. In the transverse section of the injured spinal cord shown in Fig. 1b, microstructural changes can be clearly revealed by MPM. Compared to the normal one, the primary H-shape of gray matter was destroyed after injury. And TPEF signals from the gray matter are much stronger than the white matter due to the component alterations following SCI. The striking feature of the section after injury was the hemorrhage in the central gray matter, which emits strong TPEF signals. Small and petechial hemorrhages are mainly distributed in the gray matter and the gray-white matter junction regions. The similar details of microstructure in Fig. 1a, b correlate readily with their corresponding H&E stained images shown in Fig. 1c, d, respectively.

In order to reveal the detailed microstructural changes in white and gray matter after injury, the regions labeled ROIs 1–6 in Fig. 1 are further focused and presented in Fig. 2. In the white matter, plenty of ECM mainly including hyaluronan and sulfated proteoglycans in a honeycomb pattern emit TPEF signals [18]. The cavities surrounded by ECM are mainly occupied with nerve fibers which are partly dissolved due to the paraffin embedding and then removal. In the normal white matter, nerve fibers are well-distributed surrounded by ECM (Fig. 2a). However, the nerve fibers are swollen and the number

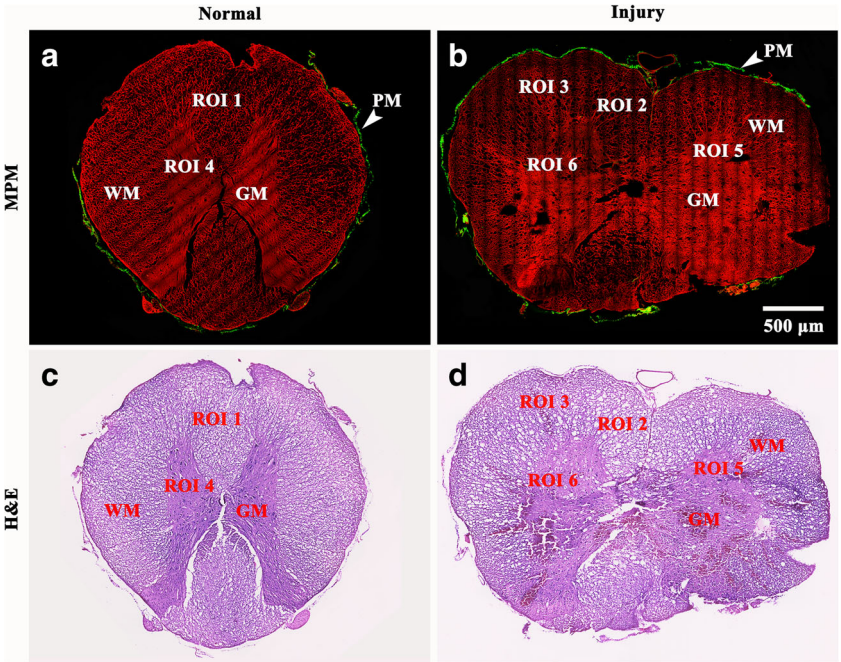

Fig. 1 **a**, **b** MPM images (×63) from the transverse section of the normal (**a**) and injured (**b**) spinal cord. **c**, **d** H&E stained images (×40) of normal (**c**) and injured (**d**) spinal cord corresponding to **a** and **b**, respectively. ROI 1 = normal white matter; ROI 2 = injured white matter without hemorrhage; ROI 3 = hemorrhagic white matter; ROI 4 = normal gray matter; ROI 5 = injured gray matter without hemorrhage; ROI 6 = hemorrhagic gray matter. WM = white matter; GM = gray matter; PM = pia matter

of nerve fibers is markedly reduced after SCI (Fig. 2b). Furthermore, hemorrhages (asterisks) in white matter are clearly identified after injury (Fig. 2c) due to the strong TPEF signals from hemoglobin in erythrocytes [19, 20]. These similar details of microstructure in Figs. 2a–c correlate readily with the corresponding H&E-stained images of Fig. 2d–f, respectively. In the gray matter, the cell bodies can be identified clearly via the TPEF imaging because nuclei appeared darker than surrounding extracellular structures [21]. It can be discovered by comparing Fig. 2g with Fig. 2h that the number of neuronal cell bodies (yellow arrowheads) are reduced. Moreover, the hemorrhages (asterisks) are also identified by MPM in Fig. 2i because the erythrocytes emitted stronger TPEF signals than the surrounding matter. These similar details of microstructure in Fig. 2g–i correlate readily with the corresponding H&E stained images of Fig. 2j–l, respectively.

To further characterize the change of white matter after injury, the cavity density and ECM content were calculated and the detail average values as well as the summary of the statistics were shown in Fig. 3. Figure 3a shows the comparison of the cavity density that is related to the density of nerve fibers in normal and injured spinal cord. The cavity density in the transverse section of

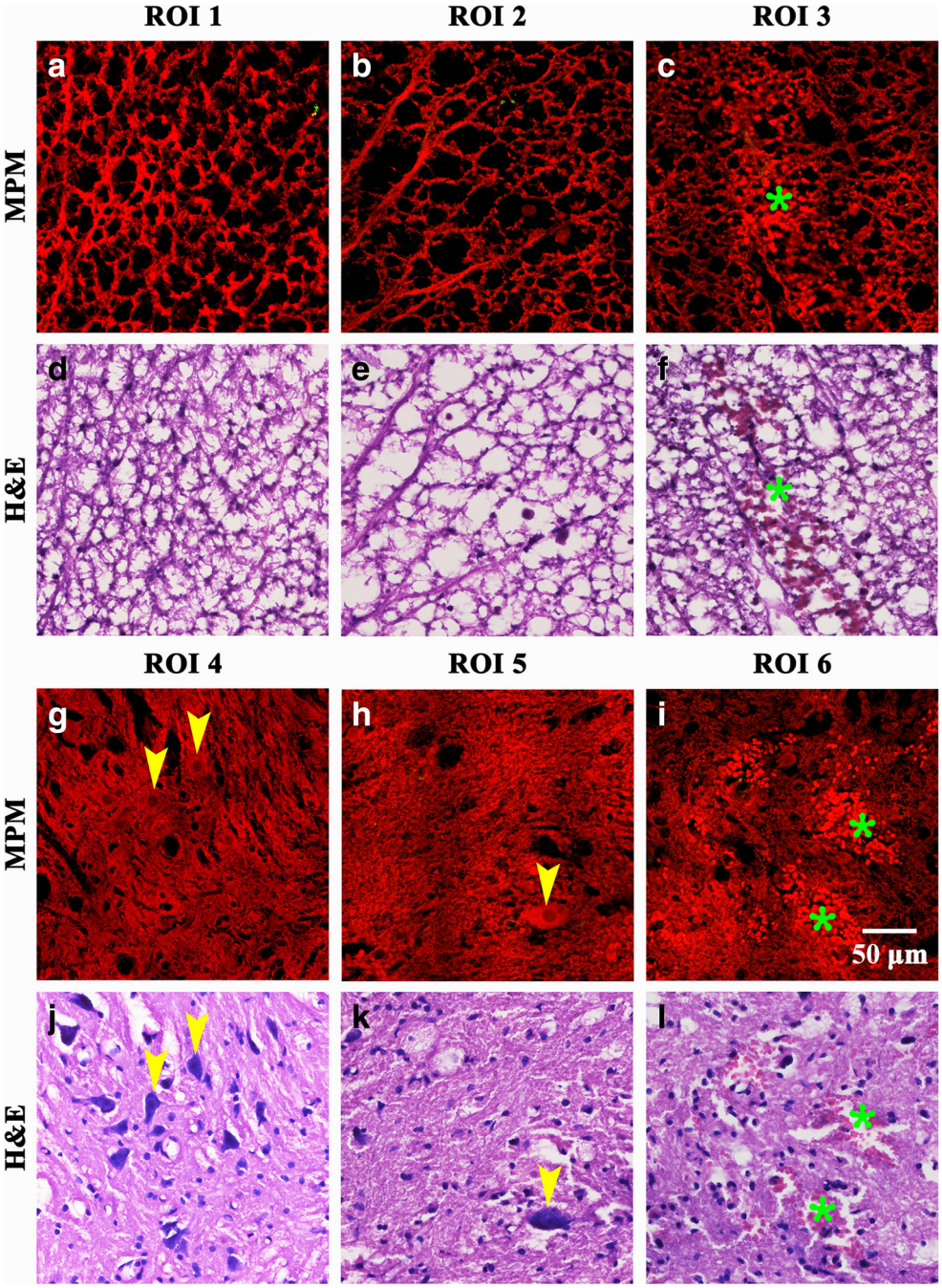

Fig. 2 Magnified MPM images (×63) and corresponding H&E images (×40) of gray and white matter in normal or injured spinal cord. **a**–**c** MPM images of normal white matter (**a**), injured white matter without hemorrhage (**b**), and hemorrhagic white matter after injury (**c**). **d**–**f** H&E stained images corresponding to MPM images (**a**–**c**). **g**–**i** MPM image of normal gray matter (**g**), injured gray matter without hemorrhage (**h**), and hemorrhagic gray matter after injury (**i**). **j**–**l** H&E stained images corresponding to the MPM images (**g**–**i**). Asterisk = erythrocytes; yellow arrowhead = neuronal cell bodies

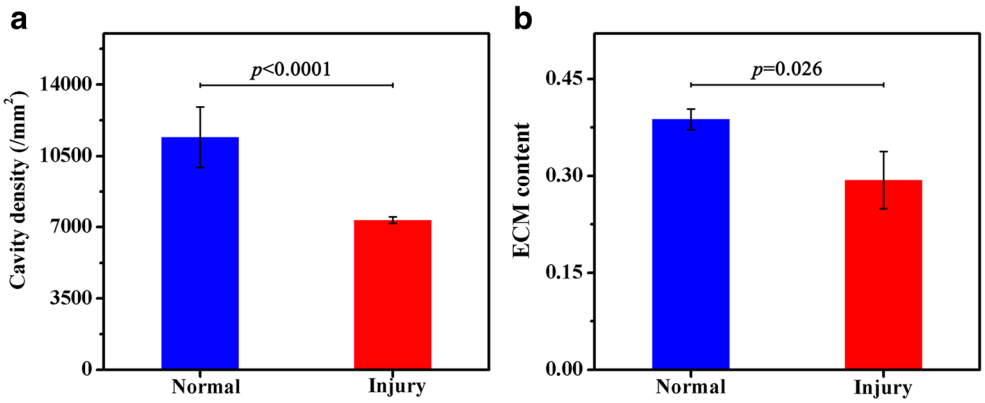

Fig. 3 Quantitation of cavity density (**a**) and ECM content (**b**) in the normal and injured white matter

the normal white matter is 11,421 ± 1480 ($p = 0.085$), while it is 7345 ± 1261 ($p = 0.610$) in the injured white matter. The result shows that the cavity density obviously decreased when the spinal cord was injured ($p < 0.0001$). Figure 3b shows the comparison of the ECM content in normal and injured white matter. The ECM content is 0.39 ± 0.02 ($p = 0.715$) in normal white matter, while it is 0.29 ± 0.04 ($p = 0.275$) in injured white matter. The result shows that the ECM content obviously decreases when the spinal cord was injured ($p = 0.026$). Therefore, the content alteration of ECM as well as the density alteration of nerve fibers are important features which may be useful indicators for quantitatively monitoring the development of SCI.

Multiphoton imaging and quantifying the longitudinal spinal cord sections

Figure 4 displays the microstructural alteration in the longitudinal section of injured spinal cord compared to the normal one. The representative MPM images and the corresponding H&E-stained images from the longitudinal sections of injured spinal cords with different proportions of gray and white matter are shown in Fig. 4. It reveals the significant microstructural changes in the injured spinal cord that consists of swollen nerve fibers and hemorrhage. Unlike what is observed in transverse section tissues, the nerve fibers in longitudinal section are longitudinally arranged. In Fig. 4a, the large-scaled MPM image mainly covers the white matter that contains a large number of nerve fibers [22]. The lower part of the image presents the white matter that was injured while the upper part is normal white matter. The upper part of Fig. 4a shows longitudinally oriented nerve fibers which depicts the well aligned and globally oriented nerve fibers of normal white matter in rat spinal cord tissue [23]. While the lower section of Fig. 4a shows that the well-aligned nerve fibers were destroyed in the injured white matter. In addition, the striking feature of hemorrhages was identified in the spinal cord after

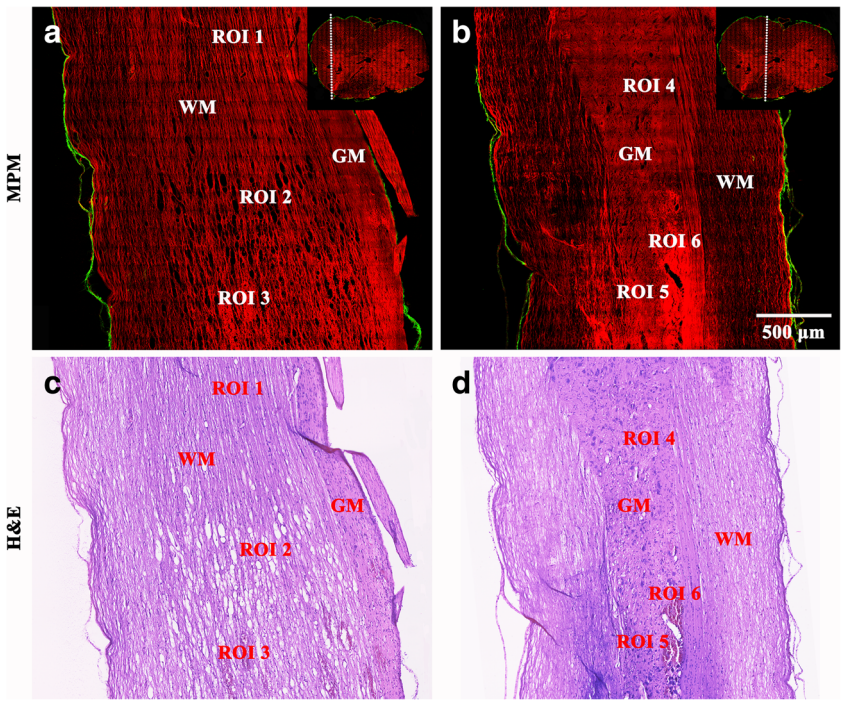

Fig. 4 MPM images of longitudinal sections including the normal (upper) and injured regions (lower) at two various sites: **a** MPM image of normal white matter and injured white matter; **b** MPM image of normal gray matter and injured gray matter. The inset images display that longitudinal section was obtained from the location marked with dotted line at the transversal section. **c**, **d** H&E stained images correspond to **a** and **b**, respectively. ROI 1 = normal white matter; ROI 2 = injured white matter without hemorrhage; ROI 3 = hemorrhagic white matter; ROI 4 = normal gray matter; ROI 5 = injured gray matter without hemorrhage; ROI 6 = hemorrhagic gray matter

injury which emits strong TPEF signals. In the spinal cord, the gray and white matters are easily discerned. In Fig. 4b, the large-scaled MPM image consists of central gray matter and bilateral white matter. The image shows that the normal gray matter is in the upper part of the image and the injured gray matter is in the lower part. Compared to the normal one in the upper part, TPEF signals from the gray matter in the lower part are much stronger due to the hemorrhage following SCI. The similar details of microstructure in Fig. 4a, b correlate readily with their corresponding H&E-stained images presented in Fig. 4c, d, respectively.

In order to reveal the detailed microstructural changes in longitudinal section of gray and white matter after injury, the regions labeled ROIs 1–6 in Fig. 4 are further focused and presented in Fig. 5. The nerve fibers (green arrowhead) are well-distributed and globally oriented in the normal white matter, as shown in Fig. 5a. The ECM surrounds the nerve fibers, which are longitudinally arranged and aligned with the nerve fibers in white matter. Oligodendrocytes (yellow arrowhead) are found throughout both the gray and white matter of the entire CNS. Especially in the white matter, these cells are more densely distributed appearing like beads on a string [24].

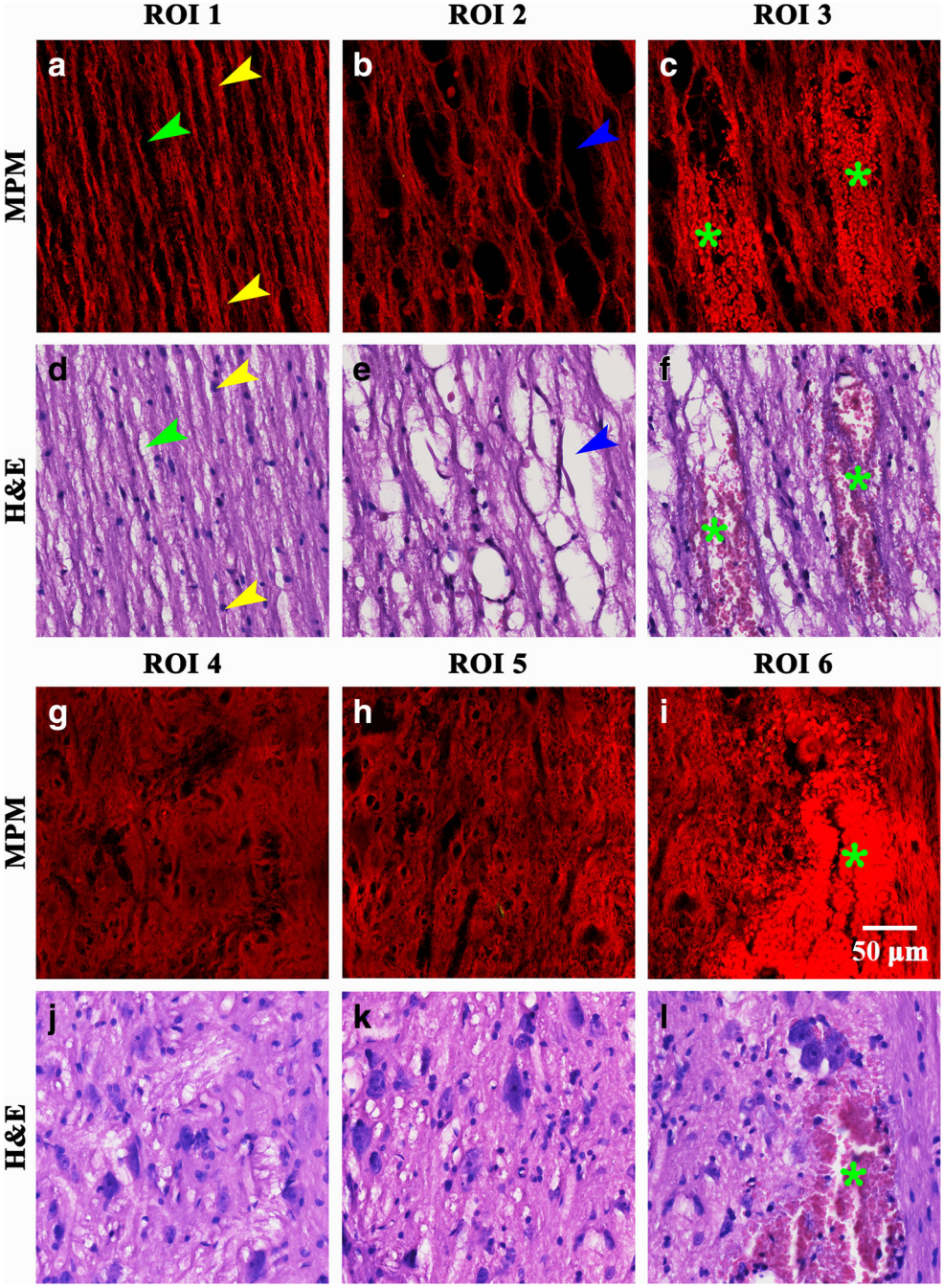

Fig. 5 Magnified MPM images (×63) and corresponding H&E images (×40) of gray and white matter in longitudinal section of normal or injured spinal cord. **a**–**c** MPM images of normal white matter (**a**), injured white matter without hemorrhage (**b**), and hemorrhagic white matter after injury (**c**). **d**–**f** H&E stained images corresponding to MPM images (**a**–**c**). **g**–**i** MPM image of normal gray matter (**g**), injured gray matter without hemorrhage (**h**), and hemorrhagic gray matter after injury (**i**). **j**–**l** H&E stained images corresponding to the MPM images (**g**–**i**). Asterisk = erythrocytes; blue arrowhead = swollen nerve fiber; green arrowhead = normal nerve fiber; yellow arrowhead = oligodendrocyte

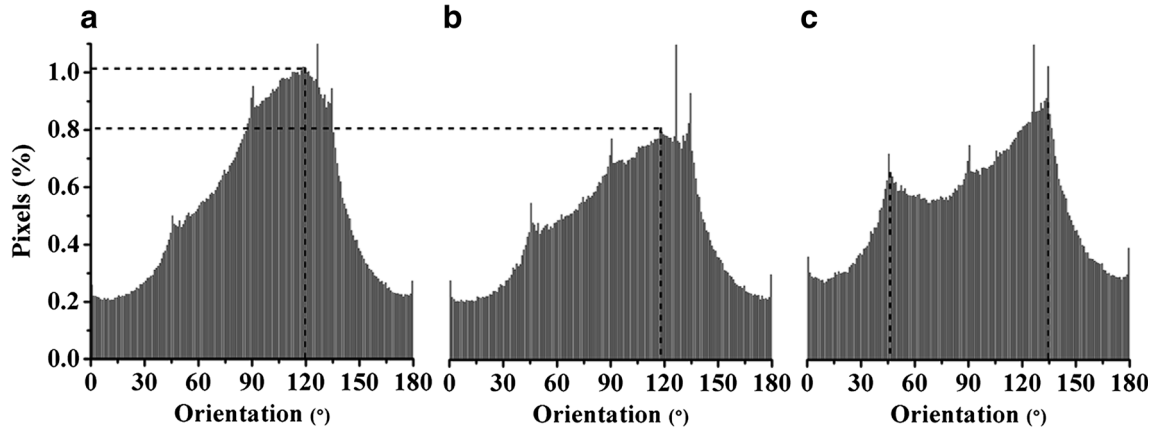

Fig. 6 The orientation distribution of ECM in normal case (**a**), swollen white matter (**b**), and hemorrhagic white matter (**c**), corresponding to Fig. 5a–c

However, there are edema, hemorrhages, and irregular alignment of ECM in the white matter of the injured spinal cord [25]. The morphological features of white matter in the normal and injury white matter are significant difference. In the normal white matter (Fig. 5a), the ECM appear straighter and form fibers with better orientation, while in the injured white matter (Fig. 5b), ECM present in a random arrangement due to the swollen nerve fibers (blue arrowhead). Comparing Fig. 5a to Fig. 5b, MPM images indicate that loss of nerve fibers was apparent in injured white matter, as previously reported [26]. In addition, the hemorrhages (asterisk) are clearly identified in Fig. 5c due to the strong TPEF signals from the erythrocytes. Therefore, nerve fiber and ECM orientation mapping may offer a new perspective to evaluate white matter disorders [27]. The similar details of microstructure in Fig. 5a–c correlate readily with their corresponding H&E stained images presented in Fig. 5d–f, respectively. In Fig. 5g, the gray matter was normal. However, there were some spotty hemorrhage areas in the injured gray matter (Fig. 5i). The hemorrhages (asterisk) can be identified by MPM in Fig. 5i because the erythrocytes emitted stronger TPEF signals than the surrounding cells and ECM [28]. Besides, there is no obvious morphological difference between the normal gray matter and the gray matter adjacent to the injury site. The similar details of microstructure in Fig. 5g–i correlate readily with their corresponding H&E-stained images presented in Fig. 5j–l, respectively.

In order to quantitatively describe the alterations of white matter after injury, the orientation and content of ECM were evaluated. The orientations of ECM in normal and injured white matter were quantified by using a weighted orientation vector summation algorithm [15]. Figure 6 shows the results of the orientation distributions in the normal (Fig. 6a), hemorrhagic (Fig. 6b), and swollen white matter (Fig. 6c). The orientation distribution of the normal case (Fig. 6a) showed one peak at approximately 120°, indicating that most of the ECM is preferred in this orientation. The orientation distribution of the swollen white matter (Fig. 6b) presents a similar pattern to the normal case in angle, showing one peak at approximately 120°. But the percentage of the pixels at the peak in swollen white matter are smaller compared with the normal case, indicating that the original orientation in the normal case changes in the swollen white matter. However, the orientation distribution of the hemorrhagic white matter (Fig. 6c) presents two peaks at approximately 45° and 135°, declaring that there are two main orientations of the ECM dominated the alignment. These results showed that the ECM in the hemorrhagic and swollen white matter are less oriented than that in the normal case, and the orientation in the hemorrhagic white matter presents most inconspicuous.

Figure 7 presents the detail values of averaged ECM content as well as the summary of the statistics, showing 0.68 ± 0.04 ($p = 0.493$) and 0.49 ± 0.01 ($p = 0.98$) in normal and injured white matter, respectively. Consequently, the obvious orientation and decreased content of ECM in longitudinal section after SCI are important features which may be useful indicators for quantitatively monitoring the development of SCI.

SCI involves a number of processes and leads to massive neuronal death and ECM composition alteration. Spinal imaging plays an essential role in the diagnosis, treatment, and rehabilitation of patients with SCI. MPM, based on the advancement of the field of nonlinear optics and femtosecond

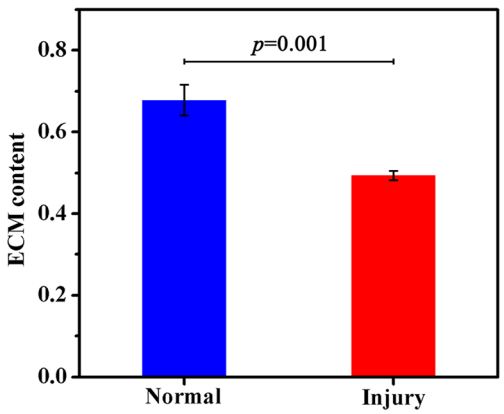

Fig. 7 The quantitation of ECM content in white matter from normal and injury spinal cord

lasers, can provide detailed information about tissue architecture using a combination of autofluorescence from cells and SHG signal from collagen and nerve fibers [12, 29]. In this study, MPM were employed to visualize the microstructural alteration of nerve fibers and ECM following SCI without any labeling agent. Since morphology examination by histology remains the golden standard, the morphological features between MPM imaging and H&E-stained imaging were compared. And the results showed that MPM images were comparable to H&E images. Moreover, quantitative information of nerve fibers and ECM changes were also provided including the density of nerve fibers and the orientation and content of ECM. The objective measurement of changes in morphology of nerve fibers and ECM will provide a useful reference for better understanding of the traumatic insult and efficacy of potential therapeutics. Therefore, our results demonstrated the feasibility to use MPM to image and quantify the morphological features of cells and matrix following SCI without need of special stains and can significantly save time compared to time-consuming H&E staining. Thus, it reserves the potential of in vivo imaging as an in situ histological tool, allowing the continual and timely examination of SCI status. Combined with the puncture technique and optical fiber [30], MPM may be found application in in vivo monitoring and providing results quickly in patients suffering SCI that immediately guides the therapeutic approach.

Conclusions

In conclusion, the noninvasive nature of MPM, coupled to its high-resolution capacity, shows significant clinical potential as a tool for optical biopsies. With the future development, we foresee promising applications of the MPM technique for in vivo assessment of SCI or diseases.

Funding information The work was supported by the Changjiang Scholars Program and the University Innovative Research Team (grant no. IRT_15R10), the National Natural Science Foundation of China (grant nos. 81671730), the Natural Science Foundation of Fujian Province (2015J01241), and a grant from the Education Bureau of Fujian Province (grant no. JA13060).

Compliance with ethical standards

Conflict of interest The authors declare that they have no competing interests.

Ethical approval The experimental procedures with rats were conducted according to the Guide for Care and Use of Laboratory Animals and approved by the Animal Care and Use Committee in Fujian Medical University.

Informed consent It does not apply, since the study was developed with Sprague-Dawley rats.

References

1. Galli R, Uckermann O, Winterhalder MJ, Sitoci-Ficici KH, Geiger KD, Koch E, Schackert G, Zumbusch A, Steiner G, Kirsch M (2012) Vibrational spectroscopic imaging and multiphoton microscopy of spinal cord injury. Anal Chem 84:8707–8714
2. Galtrey CM, Kwok JC, Carulli D, Rhodes KE, Fawcett JW (2008) Distribution and synthesis of extracellular matrix proteoglycans, hyaluronan, link proteins and tenascin-R in the rat spinal cord. Eur J Neurosci 27:1373–1390
3. Wiese S, Faissner A (2015) The role of extracellular matrix in spinal cord development. Exp Neurol 274:90–99
4. Gaudet AD, Popovich PG (2014) Extracellular matrix regulation of inflammation in the healthy and injured spinal cord. Exp Neurol 258:24–34
5. Ellingson BM, Salamon N, Holly LT (2014) Imaging techniques in spinal cord injury. World Neurosurg 82:1351–1358
6. Powers BE, Sellers DL, Lovelett EA, Cheung W, Aalami SP, Zapertov N, Maris DO, Horner PJ (2013) Remyelination reporter reveals prolonged refinement of spontaneously regenerated myelin. Proc Natl Acad Sci U S A 110:4075–4080
7. Petersen JA, Wilm BJ, von Meyenburg J, Schubert M, Seifert B, Najafi Y, Dietz V, Kollias S (2012) Chronic cervical spinal cord injury: DTI correlates with clinical and electrophysiological measures. J Neurotrauma 29:1556–1566
8. Wang M, Dai Y, Han Y, Haacke EM, Dai J, Shi D (2011) Susceptibility weighted imaging in detecting hemorrhage in acute cervical spinal cord injury. Magn Reson Imaging 29:365–373
9. Kang CE, Clarkson R, Tator CH, Yeung IW, Shoichet MS (2010) Spinal cord blood flow and blood vessel permeability measured by dynamic computed tomography imaging in rats after localized delivery of fibroblast growth factor. J Neurotrauma 27:2041–2053
10. Zoumi A, Yeh A, Tromberg BJ (2002) Imaging cells and extracellular matrix in vivo by using second-harmonic generation and two photon excited fluorescence. Proc Natl Acad Sci U S A 99:11014e9
11. Uckermann O, Galli R, Beiermeister R, Sitoci-Ficici KH, Later R, Leipnitz E, Neuwirth A, Chavakis T, Koch E, Schackert G, Steiner G, Kirsch M (2015) Endogenous two-photon excited fluorescence provides label-free visualization of the inflammatory response in the rodent spinal cord. Biomed Res Int 2015:859084
12. Israel JS, Esquibel CR, Dingle AM, Liu Y, Keikhosravi A, Pisaniello JA, Hesse MA, Brodnick SK, Novello J, Krugner-Higby L, Williams JC, Eliceiri KW, Poore SO (2017) Quantification of collagen organization after nerve repair. Plast Reconstr Surg Glob Open 5:e1586
13. Noble LJ, Wrathall JR (1985) Spinal cord contusion in the rat: morphometric analyses of alterations in the spinal cord. Exp Neurol 88:135–149
14. Zhu X, Tang Y, Chen J, Xiong S, Zhuo S (2013) Monitoring wound healing of elastic cartilage using multiphoton microscopy. Osteoarthr Cartilage 21:1799–1806
15. Quinn KP, Georgakoudi I (2013) Rapid quantification of pixel-wise fiber orientation data in micrographs. J Biomed Opt 18: 046003–046003
16. Shapiro SS, Wilk MB (1965) An analysis of variance test for normality (complete samples). Biometrika 52:591–611
17. Nam MH, Baek M, Lim J, Lee S, Yoon J, Kim J, Soh KS (2014) Discovery of a novel fibrous tissue in the spinal pia mater by polarized light microscopy. Connect Tissue Res 55:147–155
18. Bignami A, Asher R, Perides G (1992) The extracellular matrix of rat spinal cord: a comparative study on the localization of hyaluronic acid, glial hyaluronate-binding protein, and chondroitin sulfate proteoglycan. Exp Neurol 117:90–93

19. Li D, Zheng W, Zeng Y, Luo Y, Qu JY (2011) Two-photon excited hemoglobin fluorescence provides contrast mechanism for label-free imaging of microvasculature in vivo. Opt Lett 36:834–836
20. Saytashev I, Glenn R, Murashova GA, Osseiran S, Spence D, Evans CL, Dantus M (2016) Multiphoton excited hemoglobin fluorescence and third harmonic generation for non-invasive microscopy of stored blood. Biomed Opt Express 7:3449–3460
21. Liao CX, Wang ZY, Zhou Y, Zhou LQ, Zhu XQ, Liu WG, Chen JX (2017) Label-free identification of the microstructure of rat spinal cords based on nonlinear optical microscopy. J Microsc 267:143–149
22. Waxman SG, Kocsis JD, Stys PK (1995) The axon: structure, function, and pathophysiology. Oxford University Press, Oxford
23. Wang F, Bélanger E, Paquet ME, Côté DC, De Koninck Y (2016) Probing pain pathways with light. Neuroscience 338:248–271
24. Johansen-Berg H, Behrens TE (2013) Diffusion MRI: from quantitative measurement to in vivo neuroanatomy. Academic press, San Diego
25. Cheran S, Shanmuganathan K, Zhuo J, Mirvis SE, Aarabi B, Alexander MT, Gullapalli RP (2011) Correlation of MR diffusion tensor imaging parameters with ASIA motor scores in hemorrhagic and nonhemorrhagic acute spinal cord injury. J Neurotrauma 28: 1881–1892
26. Quencer RM, Bunge RP, Egnor M, Green BA, Puckett W, Naidich TP, Post MJD, Norenberg M (1992) Acute traumatic central cord syndrome: MRI-pathological correlations. Neuroradiology 34:85–94
27. Douek P, Turner R, Pekar J, Patronas N, Le Bihan D (1991) MR color mapping of myelin fiber orientation. J Comput Assist Tomogr 15:923–929
28. Li LM, Li JB, Zhu Y, Fan GY (2010) Soluble complement receptor type 1 inhibits complement system activation and improves motor function in acute spinal cord injury. Spinal Cord 48:105–111
29. Dray C, Rougon G, Debarbieux F (2009) Quantitative analysis by in vivo imaging of the dynamics of vascular and axonal networks in injured mouse spinal cord. Proc Natl Acad Sci U S A 106:9459–9464
30. Helmchen F, Denk W, Kerr JN (2013) Miniaturization of two-photon microscopy for imaging in freely moving animals. Cold Spring Harb Protoc 2013:904–913